ARL-TR-10430 • Sep 2026

Development of Aluminum–Cerium–Nickel–Magnesium (Al-Ce-Ni-Mg) Based Alloys

by Taylor W. Cain and Jon-Erik Mogonye

NOTICES

Disclaimers

ARL-TR-10430 ● SEP 2026

Development of Aluminum–Cerium–Nickel–Magnesium (Al-Ce-Ni-Mg) Based Alloys

Taylor W. Cain and Jon-Erik Mogonye
DEVCOM Army Research Laboratory

REPORT DOCUMENTATION PAGE

1. REPORT DATE	2. REPORT TYPE	3. DATES COVERED START DATE	3. DATES COVERED END DATE
September 2026	Technical Report	1 November 2020	1 December 2023

4. TITLE AND SUBTITLE
Development of Aluminum–Cerium–Nickel–Magnesium (Al-Ce-Ni-Mg) Based Alloys

5a. CONTRACT NUMBER	5b. GRANT NUMBER	5c. PROGRAM ELEMENT NUMBER

5d. PROJECT NUMBER	5e. TASK NUMBER	5f. WORK UNIT NUMBER

6. AUTHOR(S)
Taylor W. Cain and Jon-Erik Mogonye

7. PERFORMING ORGANIZATION NAME(S) AND ADDRESS(ES)	8. PERFORMING ORGANIZATION REPORT NUMBER
DEVCOM Army Research Laboratory ATTN: FCDD-RLA-MF Aberdeen Proving Ground, MD 21005	ARL-TR-10430

9. SPONSORING/MONITORING AGENCY NAME(S) AND ADDRESS(ES)	10. SPONSOR/MONITOR'S ACRONYM(S)	11. SPONSOR/MONITOR'S REPORT NUMBER(S)

12. DISTRIBUTION/AVAILABILITY STATEMENT
DISTRIBUTION STATEMENT A. Approved for public release: distribution unlimited.

13. SUPPLEMENTARY NOTES
ORCIDs: Taylor W. Cain, 0000-0002-6621-914X; Jon-Erik Mogonye, 0000-0002-7508-083X

14. ABSTRACT
This technical report explores the potential of near-eutectic aluminum–cerium–nickel–magnesium (Al-Ce-Ni-Mg) alloys as a new class of cast aluminum alloys. Thirteen unique compositions were investigated via microscopy and hardness measurements to determine an alloy composition for scaled-up evaluation. A simple hardness model was applied to the alloy system to determine the relative strengthening contributions of different phases as part of the down-selection criteria. An Al-8.41Ce-2.15Ni-4Mg wedge casting showed good strength retention as a function of solidification rate and is suggested as a candidate for further research efforts.

15. SUBJECT TERMS
aluminum casting, aluminum alloy, eutectic alloy, aluminum-cerium alloy, Al-Ce-Ni-Mg, aluminum-cerium-nickel-magnesium alloy, Mechanical Sciences, Sciences of Extreme Materials

16. SECURITY CLASSIFICATION OF: a. REPORT	b. ABSTRACT	C. THIS PAGE	17. LIMITATION OF ABSTRACT	18. NUMBER OF PAGES
UNCLASSIFIED	UNCLASSIFIED	UNCLASSIFIED	UU	32

19a. NAME OF RESPONSIBLE PERSON	19b. PHONE NUMBER *(Include area code)*
Taylor W. Cain	(520) 691-5035

STANDARD FORM 298 (REV. 5/2020)
Prescribed by ANSI Std. Z39.18

Contents

List of Figures

List of Tables

1. Introduction

Recent research efforts have found aluminum–cerium (Al-Ce) based alloys to be an emerging technology with rapid development both as a cast alloy and through additively manufactured methods. The majority of research on Al-Ce based alloys has occurred within the last 5 years where the aluminum–cerium–magnesium (Al-Ce-Mg),[1–6] aluminum–cerium–nickel (Al-Ce-Ni),[7–9] aluminum–cerium–manganese (Al-Ce-Mn),[10–15] and aluminum–cerium–nickel–manganese (Al-Ce-Ni-Mn)[16–22] systems have received the broadest amount of attention. These alloys are noted for their high volume fraction of thermally stable $Al_{11}Ce_3$ eutectic phase, which provides excellent room temperature and high-temperature mechanical properties for Al alloys, especially when additively manufactured or when alloyed with $L1_2$ nanoprecipitate forming elements such as scandium (Sc) and zirconium (Zr).[23–26] Indeed, prior research at the U.S. Army Combat Capabilities Development Command (DEVCOM) Army Research Laboratory (ARL) has explored precipitation hardenable aluminum–cerium–magnesium–zinc (Al-Ce-Mg-Zn) based alloys where excellent precipitation hardenability was discovered but rapid overaging was observed at temperatures over 300 °C. While precipitation-hardenable Al-Ce alloys present the greatest strengthening effect, solid solution–strengthened Al-Ce based alloys remain of interest. There is a paucity of data in current literature on Al-Ce-Ni-Mg based alloys with only a few very recent reports having been published.[27,28] Shen et al.[27] determined the effect of Mg additions up to 1 wt% on the eutectic Al-13Ce-4Ni system at room temperature and 300 °C, while Park et al.[28] determined the microstructure creep relationship for Al-7Ce-3Ni-8Mg alloys fabricated by laser powder bed fusion.

The goal of this research was to study the effect of Mg on microstructure and hardness of near-eutectic Al-Ce-Ni based alloys. This was accomplished by first screening a range of alloy composition using small-scale button melts characterized by X-ray diffraction (XRD), scanning electron microscopy (SEM), and hardness measurements. A down-selected alloy composition was produced in a wedge casting to evaluate solidification rate effects on microstructure and mechanical properties.

2. Methods

2.1 Fabrication of Button Alloys

Al-Ce-Ni-Mg alloy buttons were produced by first casting a “mother” alloy for which Mg additions were made. The mother alloy was produced as a cast rod using

99.99% pure Al (Alfa Aesar), commercial purity Al-20 Ni (Belmont Metals), and an in-house Al-20Ce master alloy made from pure Al and a 99.95% Al-75Ce master alloy (American Elements). Three mother alloy rods were produced with the intended compositions shown in Table 1. The alloy CN92 with a constant ratio 1.8:1.1 at% Ce:Ni was first selected as a basis alloy that would be hypoeutectic with the first solid formed as α-Al as shown by the liquidus projection in Figure 1. From this alloy, two additional compositions following a cluster line from the eutectic point were made with ±20% (Ce + Ni) from CN92. The alloy charge for each mother alloy was melted using an Indutherm VTC 800 V/Ti vacuum induction melting furnace under an atmosphere of 99.99% pure argon (Ar). After all charge had melted, the furnace was held for 15 min at 850 °C to ensure good mixing under the induction field. The melt temperature was then reduced to 810 °C, mechanically stirred, and slag removed before casting into a 35-mm-diameter graphite mold encased by olivine sand that was preheated to 200 °C. The as-solidified mother alloy rods were then sectioned for production of button alloys.

Table 1. Intended composition of Al-Ce-Ni alloys used as a base alloy for making Al-Ce-Ni-Mg buttons.

Alloy	Al (wt%)	Ce (wt%)	Ni (wt%)	Ce:Ni (at%)
CN72	91.23	6.98	1.79	1.44:0.88
CN92	89	8.76	2.24	1.8:1.1
CN103	87.15	10.22	2.63	2.16:1.32

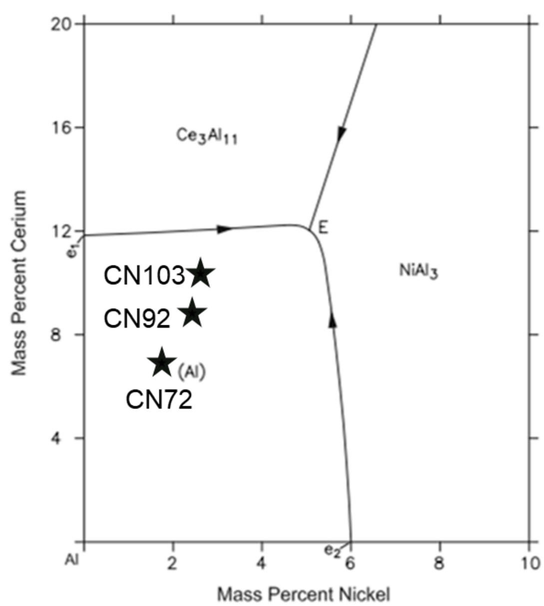

Figure 1. Liquidus projection of the Al-Ce-Ni system adapted from Raghavan.[8]

Button alloys, with a target mass of 20–25 g, were produced via induction melting in a 25-kW vacuum induction melting (VIM) furnace with an output frequency of 30–80 kHz. The alloy charge was loaded into a graphite crucible contained within porous alumina refractory insulation and quartz tube that was sealed by a vacuum flange assembly as described in ARL-TN-1091.[29] After loading the charge, the sealed vacuum flange tube assembly was removed from the glovebox and placed in the VIM. Alloys were melted under a positive flow of ultra-high-purity helium (He; 99.999%), held at 750 °C for 10 min after all charge had melted, and allowed to furnace cool. For this investigation 99.9% pure Mg (US Magnesium LLC) additions were made to each mother alloy to produce the final target compositions shown in Table 2 in addition to buttons without Mg. Additional buttons outside of this initial test matrix were produced following the same method as given in Table 3.

Table 2. Intended alloy composition of Al-Ce-Ni-Mg button test matrix.

Alloy	wt%			at%			
	Ce	Ni	Mg	Ce	Ni	Mg	Ce+Ni
CN72-B1	6.98	1.79	0	1.44	0.88	0	2.32
CNM722-B1	6.84	1.75	2	1.4	0.86	2.37	2.26
CNM724-B1	6.7	1.72	4	1.37	0.84	4.72	2.21
CNM726-B1	6.57	1.68	6	1.34	0.82	7.05	2.16
CN92-B1	8.76	2.24	0	1.8	1.1	0	2.90
CNM922-B1	8.58	2.2	2	1.79	1.10	2.41	2.89
CNM924-B1	8.41	2.15	4	1.75	1.07	4.80	2.82
CNM926-B1	8.23	2.11	6	1.71	1.04	7.17	2.75
CN103-B1	10.28	2.63	0	2.16	1.32	0	3.48
CNM1031-B1	10.17	2.61	1	2.16	1.33	1.23	3.49
CNM1032-B1	10.06	2.58	2	2.14	1.31	2.45	3.44
CNM1036-B1	9.65	2.47	6	2.03	1.24	7.28	3.27

Table 3. Nominal compositions of additional buttons made with 6 wt% Mg.

Alloy	wt%			at%			
	Ce	Ni	Mg	Ce	Ni	Mg	Ce/Ni
CNM716 B1	6.89	1.42	6	1.30	0.65	6.63	2.00
CNM726 B2	7.00	2.1	6	1.35	0.97	6.67	1.40
CNM816 B1	7.88	0.94	6	1.52	0.43	6.67	3.51
CNM926-B2	9.00	1.85	6	1.76	0.86	6.77	2.04

2.2 Fabrication of Wedge Castings

A wedge casting of the down-selected alloy was produced by casting into a copper (Cu) mold preheated at 400 °C using the mold described in Figure 2. Approximately 1200 g of total charge was melted in the Indutherm VTC 800 V/Ti vacuum induction melting furnace under an atmosphere of 99.99% pure Ar. All charge was allowed to melt after being held at 800 °C for 10 min. The melt temperature was then reduced to 750 °C and held for 10 min with mechanical stirring every 5 min, after which slag was removed prior to casting.

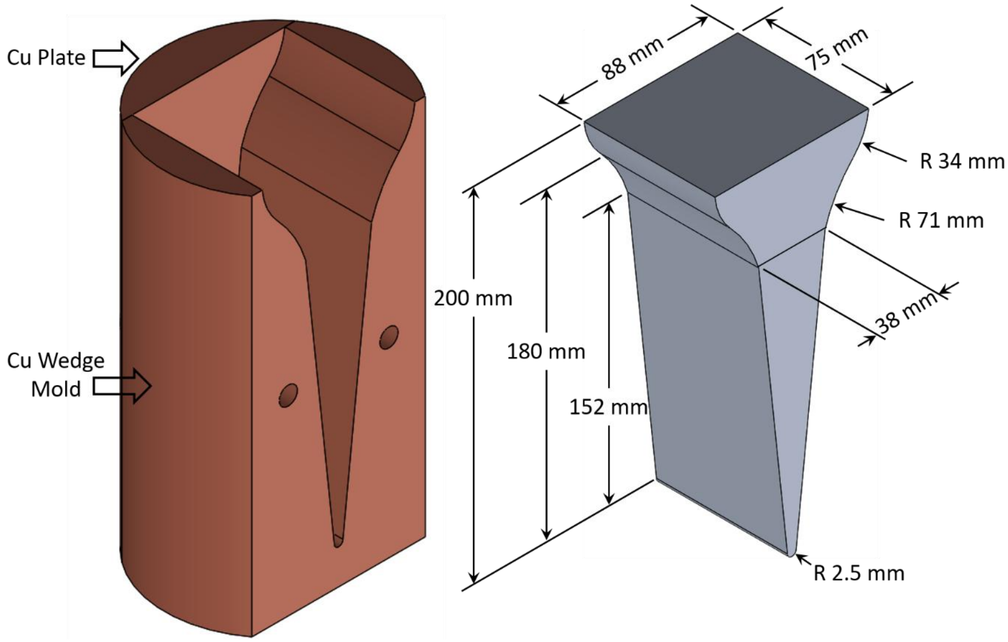

Figure 2. Schematic drawing of the Cu wedge mold with an approximate volume of 425 cm^3.

2.3 Characterization of Cast Alloys

Phase identification of samples was performed via powder XRD on a Bruker D2 Phaser with a cobalt (Co) k_α X-ray source. Samples in a Bragg–Brentano geometry were evaluated with a 2θ scan range of 15°–90°, a step size of 0.02°, and a dwell of 1 s/step. Phase identification was performed using the Bruker DIFFRAC.EVA software with the ICDD PDF-5+ 2024 database. The microstructure of samples in various conditions was characterized via SEM (Hitachi SU3500) in backscattered electron (BSE) mode together with energy-dispersive X-ray spectroscopy (EDS, Bruker QUANTAX). For SEM and hardness measurements, the samples were cold mounted in epoxy, ground with successive silicon carbide (SiC) papers to 1200-grit CAMI finish, and polished using 1- and 0.25-µm water-based diamond suspensions with the final polishing step in 0.05-µm colloidal silica.

Quantitative image analysis was performed using the Labkit multiclass segmentation plugin for Fiji[30] on at least 5 BSE images for each alloy button whose field of view was 1.270 × 0.9525 mm. The chosen images were periodically spaced from the outer edge to the center of the sample, which was deemed to provide a representative characterization of the sample. Vickers microhardness measurements were carried out on a Mitutoyo HM-200 Vickers hardness tester using a 0.3-kgf load with a 5-s load time, 10-s dwell time, and 5-s unload time.

Determination of the coefficient of thermal expansion (CTE) was performed on an Orton 2016STD on samples 0.25 inch in diameter and 1 inch in length. The machine was first calibrated and corrected to the National Institute of Standards and Technology SRM 736[31] standard profile for Cu in the range of 20–400 °C using a 99.99% pure Cu rod of the same diameter and length at a heating rate of 3 °C/min.

3. Results and Discussion

3.1 Button Melt Matrices

Powder XRD patterns for CNM buttons in the as-solidified condition are shown in Figure 3 with the intended compositions in Table 2. Pattern matching of the results show only the presence of faced-centered cubic (FCC) α-Al, orthorhombic $Al_{11}Ce_3$ phases, and orthorhombic Al_3Ni phases, indicating that the addition of Mg is found within the α-Al matrix phase. This is further indicated by a shift in the α-Al peaks to lower 2θ values as the composition of Mg increased due to an increase in lattice parameter as α-Al accommodates larger Mg atoms within the FCC lattice.

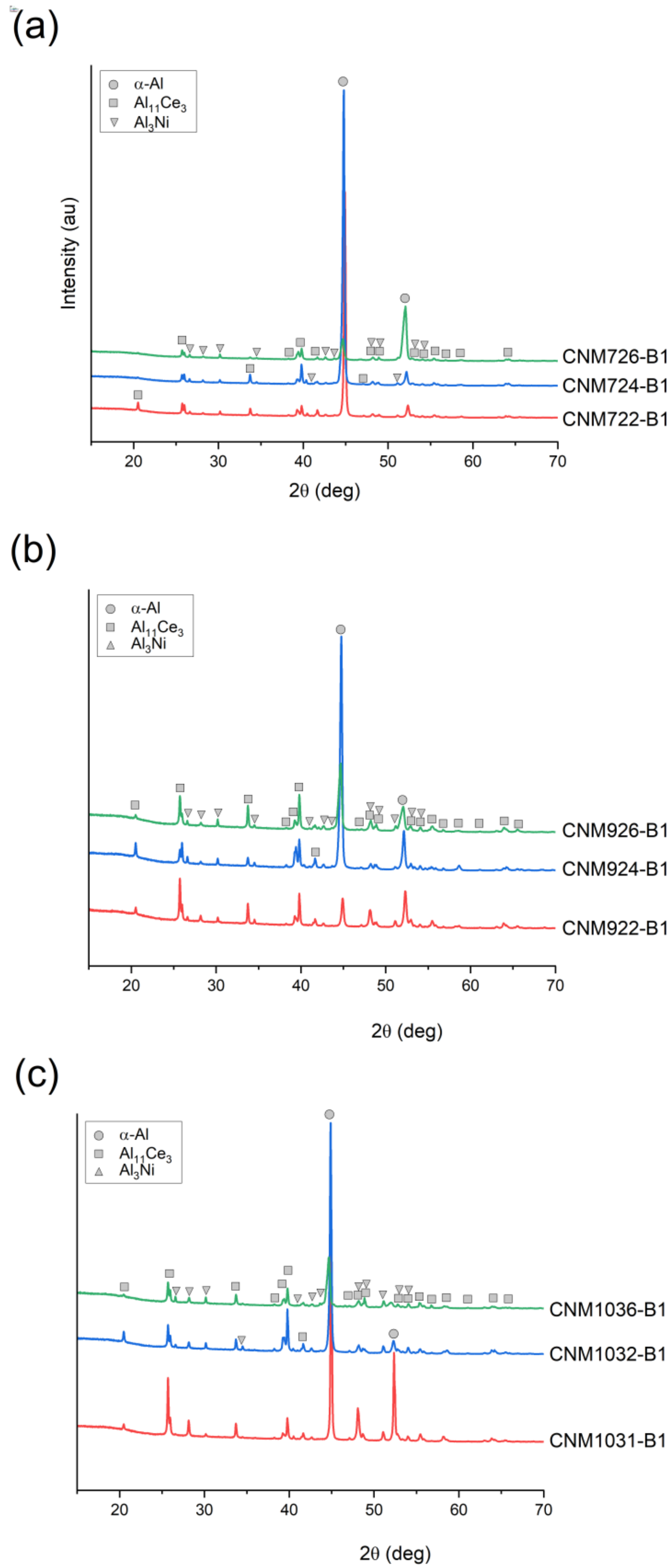

Figure 3. **Powder XRD patterns for CNM buttons in the as-solidified condition for (a) CNM72x, (b) CNM92x, and (c) CNM103x where x denotes the Mg concentration in wt%.**

The characteristic microstructure of each alloy in the as-solidified condition is shown in Figure 4 using BSE images. For all alloys, three different contrast phases were identified: the α-Al matrix, $Al_{11}Ce_3$, and Al_3Ni as confirmed by XRD. As an example, these distinct phases can be observed at higher magnification in Figure 5 for sample CNM1036-B1 via BSE imaging and corresponding energy-dispersive X-ray spectroscopy (EDS) maps in the as-solidified condition (Figure 5a) and after homogenization treatment at 475 °C for 2 h (Figure 5b). The Al_3Ni phase appears as a medium contrast phase correlated with the strong Ni k_α signal in the EDS maps while the bright contrast phase is the $Al_{11}Ce_3$ phase noted by the strong Ce k_α signal with no evidence of Ni partitioning to the bright phase. Meanwhile, the Mg signal appears locally concentrated in the as-solidified condition but without evidence of the ß-Al_3Mg_2 from XRD analysis. After homogenization, the Mg signal is observed to evenly disperse throughout the α-Al matrix, which confirms 475 °C for 2 h as an effective heat treatment schedule for homogenization of CNM alloys. Backscattered SEM images revealed a fine lamellar morphology of the Al_3Ni phase for the ternary Al-Ce-Ni alloy buttons. However, when Mg was added to the Al-Ce-Ni system, the fine lamellar structure transitioned into more of a blocky morphology with increasing Mg concentration at each Ce:Ni ratio. Increases in the Mg concentration also increased the size of the secondary phases and increased the spacing between Al_3Ni. The same trend in size and spacing was observed for $Al_{11}Ce_3$ accompanied by a change in the morphology with increasing Mg concentration such that a large blocky primary $Al_{11}Ce_3$ phase is present for CNM926, CNM1032, and CNM1036. The presence of primary $Al_{11}Ce_3$ is indicative of hypereutectic solidification with $Al_{11}Ce_3$ being the first solid formed.

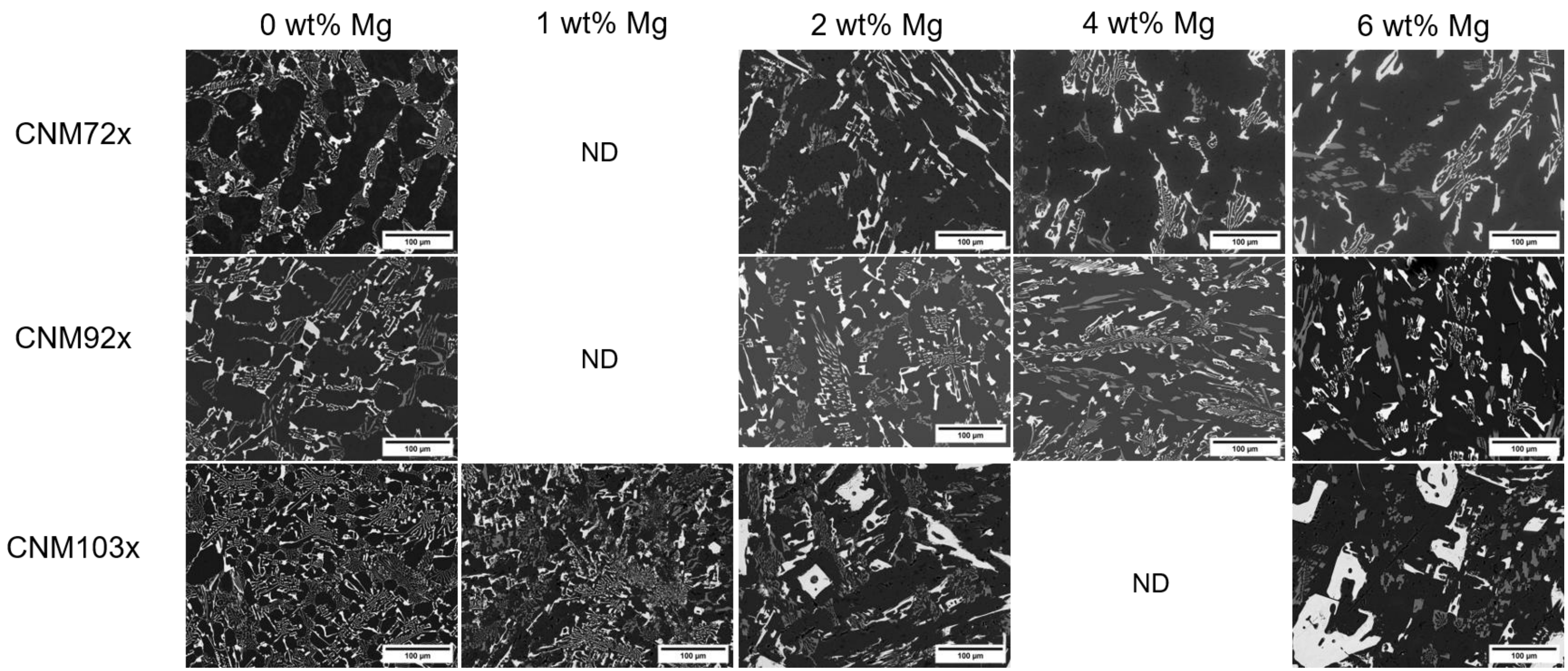

Figure 4. **Characteristic BSE images of CNM buttons in the as-solidified condition; ND indicates alloy compositions that were not produced in this study. The scale bar is 100 µm.**

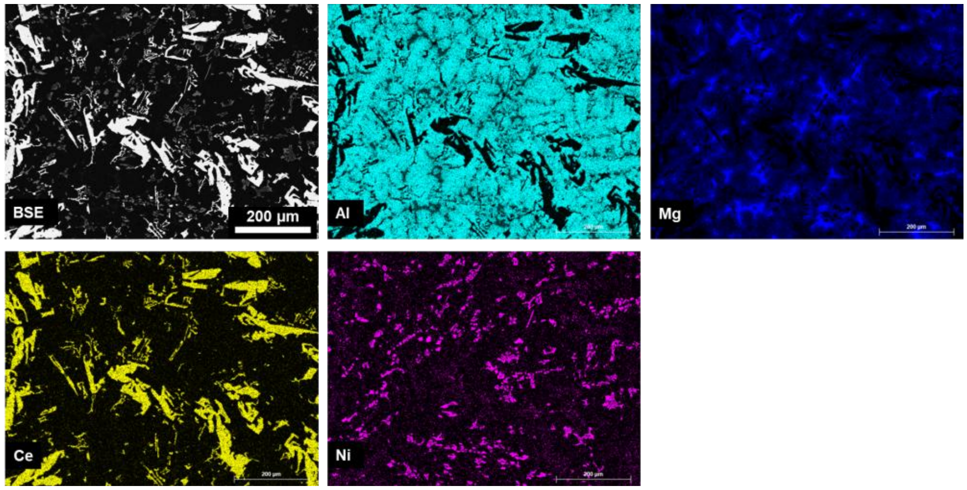

(a)

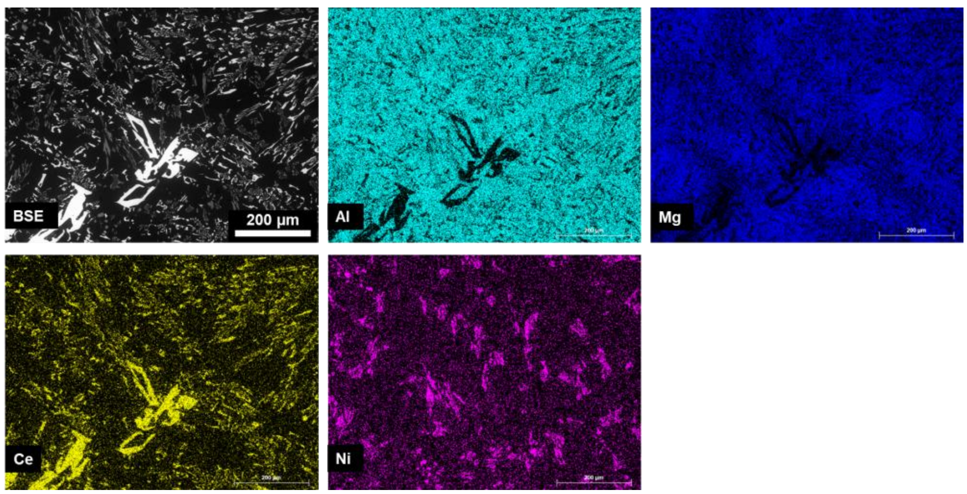

(b)

Figure 5. Backscattered SEM images of CNM1036-B1 with accompanying EDS elements maps in (a) the as-solidified condition and (b) after homogenization heat treatment of 2 h at 475 °C.

Plots of the secondary phase fraction for the CNM buttons produced in Table 2 are shown in Figure 6 for the as-solidified and homogenized condition. There were no distinguishable linear trends for Al_3Ni and $Al_{11}Ce_3$ phase fraction as a function of increasing Mg concentration in the as-solidified condition across each button ratio, while the $Al_{11}Ce_3$ phase fraction decreased with increasing Mg for each button ratio in homogenized conditions. This finding is interesting as the phase fraction was expected to be relatively stable due to the low solubility of Ni and Ce in the α-Al matrix phase, but a small decrease would be possible as the Ce and Ni concentrations become more dilute with increasing Mg additions to the mother Al-Ce-Ni rods. This data suggests local concentration variation in the mother rods used to produce the button melt samples resulting in Ce and Ni concentrations different than that intended.

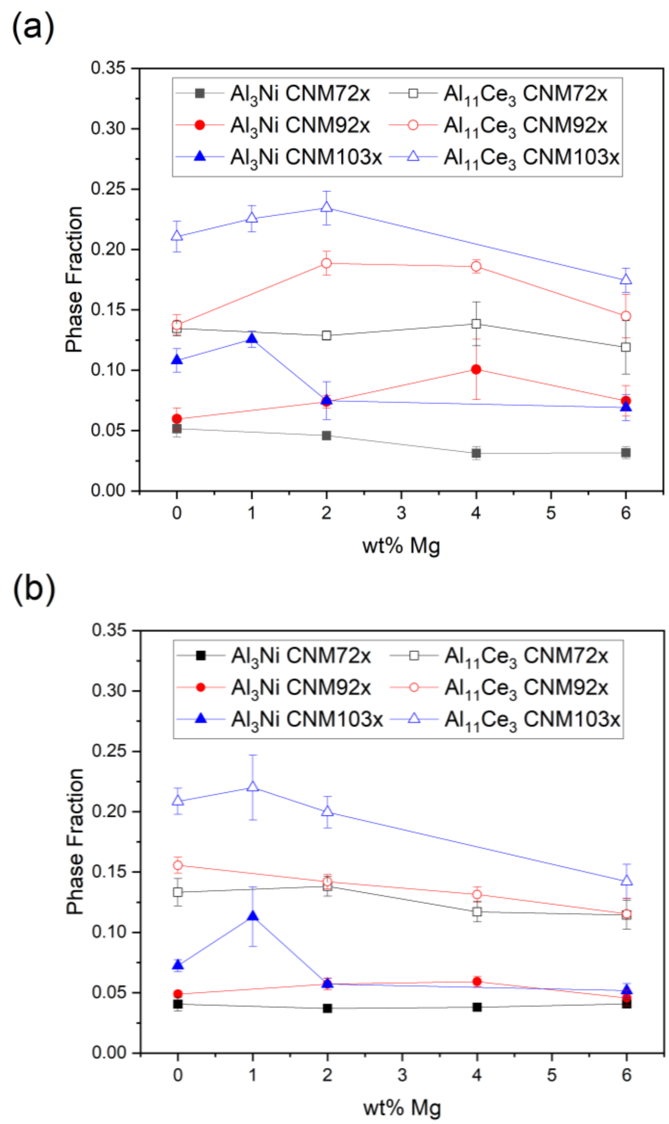

Figure 6. Phase fraction of Al_3Ni (closed symbols) and $Al_{11}Ce_3$ (open symbols) for (a) as-solidified buttons and (b) homogenized buttons as determined by quantitative image analysis.

To determine the relative effect of each alloying element on phase formation, correlation plots of area fraction of each phase and composition were made in Figure 7. First, the top-left figure shows the first-order effect of alloying element with the formation of the phase corresponding to that element, meaning that Ce is found in the $Al_{11}Ce_3$ phase, Ni is found in Al_3Ni, and Mg is found in the α-Al matrix. Linear regression performed on the data shows good correlation as indicated by the r^2 values on the plot. The slope of the linear fit for Mg is very low, indicating that it has minimal effect on the formation of α-Al while the slope for Ce is higher, indicating a stronger effect of Ce on the phase fraction of $Al_{11}Ce_3$. Meanwhile, Ni possessed the highest slope, indicating that the phase fraction of Al_3Ni is very sensitive to the Ni concentration. To explore the interplay of alloying elements on the phase formation, plots of the phase fraction of each phase versus nominal composition are given for α-Al in the top right, $Al_{11}Ce_3$ in the bottom left, and Al_3Ni in the bottom right of Figure 7. For α-Al, Mg possessed a positive slope but a poor correlation, indicating increased volume fraction of α-Al with increasing Mg concentration, while Ce and Ni both possessed a negative slope meaning increased Ni; Ce decreased the fraction of α-Al, which is expected since Ce and Ni both form secondary phases. Interestingly, the slopes indicate that the fraction of α-Al is most sensitive to Ni concentration. This is also true for the fraction of Al_3Ni and $Al_{11}Ce_3$ where small additions of Ni can facilitate greater increases in the fraction of both phases. This finding is important when thinking about the tunability of Al-Ce-Ni-Mg alloys for their mechanical properties via manipulation of the microstructure.

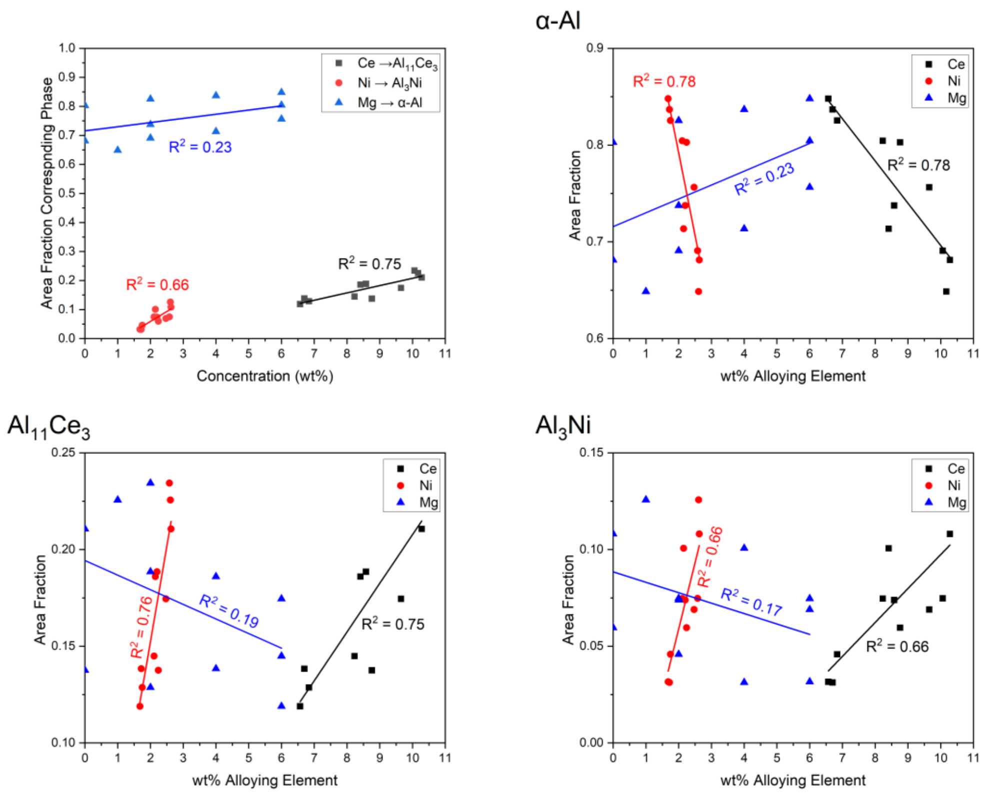

Figure 7. **Correlation plots of phase fraction vs. the wt% of each alloying element.**

The average Vickers hardness of CNM buttons is shown in Figure 8 in the as-solidified condition (Figure 8a) and after a homogenization treatment of 475 °C for 2 h (Figure 8b) where the hardness is shown as a function of Mg concentration. The plots revealed a strong solid solution strengthening effect of Mg following the typical power law behavior close to that of a square root relationship. Some variation in the hardness between the as-solidified and homogenized condition was observed but is within error, likely due to differences in the local microstructure where hardness was measured. In addition to the Mg strengthening effect, the hardness was measured to increase with increasing ratio of Ce:Ni with the highest hardness found for CNM1036.

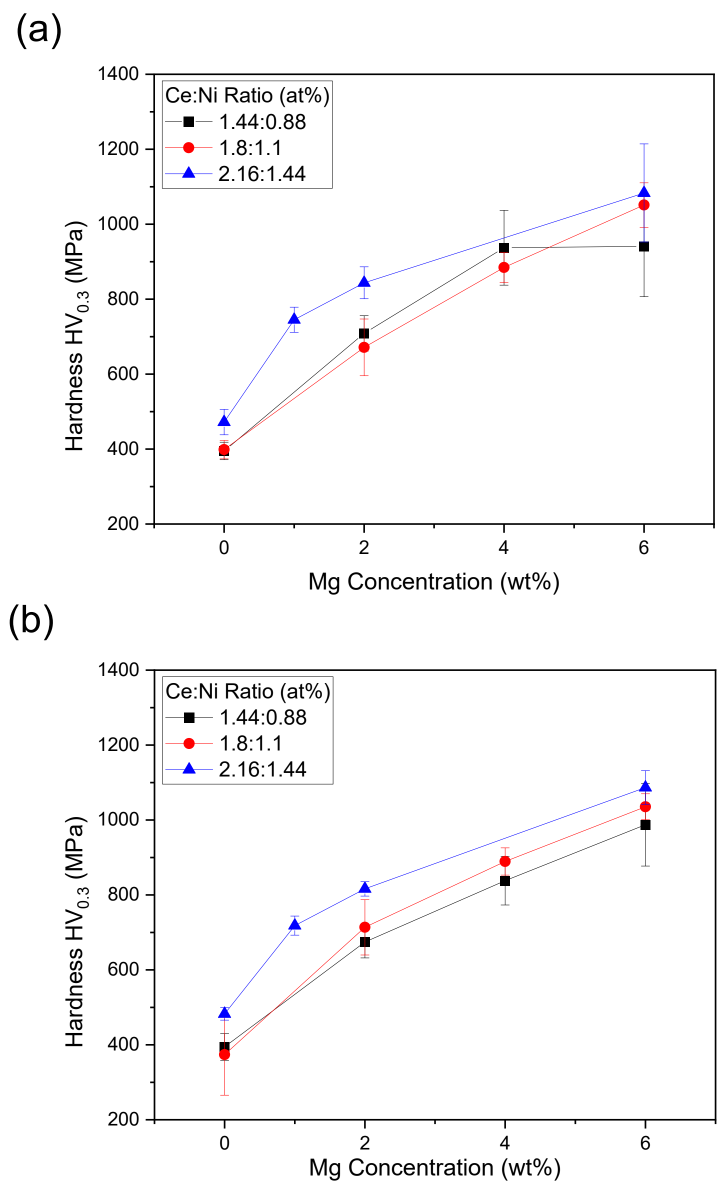

Figure 8. Vickers hardness of CNM buttons in (a) the as-solidified condition and (b) after homogenization heat treatment of 2 h at 475 °C.

In light of the hardness data and formation of $Al_{11}Ce_3$ primaries found in Figure 4, four additional buttons were produced with a constant Mg concentration of 6 wt% in an attempt to find the eutectic point of the system; 6 wt% Mg was chosen as it produced the highest hardness of those alloys in the original button matrix and therefore may be of greatest interest as an engineering material. The hardness map with accompanying BSE images is shown in Figure 9 for these additional buttons.

The hardness as a function of Ni and Ce composition showed an increase in hardness with increasing Ce and Ni content. Based on the BSE images where primary formation of $Al_{11}Ce_3$ and Al_3Ni were observed, an estimated liquidus projection was superimposed on the plot, which indicates the eutectic composition lies very close to that of CNM926-B1 but with less Ce and Ni concentration.

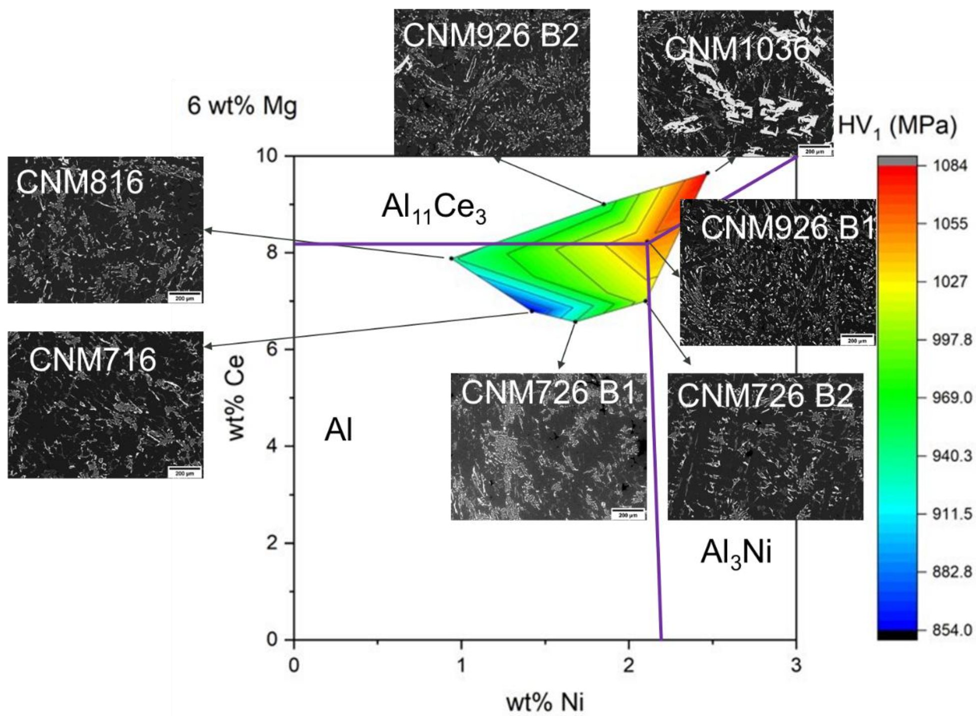

Figure 9. The estimated liquidus projection for constant Mg concentration of 6 wt%. The scale bar for each image is 200 µm.

3.2 Hardness Model

To further explore the effect of microstructure on the hardness of the Al-Ce-Ni-Mg system, regression analysis was applied to the hardness and area fraction data sets using the following simple constitutive equation where the total hardness (*VHN*) is assumed to be the sum of all strengthening components in the alloy as a fraction of their phase fraction or concentration:

$$VHN = f_{matrix}VHN_{matrix} + f_{Al_{11}Ce_3}VHN_{Al_{11}Ce_3} + f_{Al_3Ni}VHN_{Al_3Ni} \quad (1)$$

In Equation 1, f_{matrix}, $f_{Al_{11}Ce_3}$, and f_{Al_3Ni} are the area fraction of the α-matrix, $Al_{11}Ce_3$, and Al_3Ni, respectively, as determined by quantitative image analysis, while VHN_{matrix}, $VHN_{Al_{11}Ce_3}$, and VHN_{Al_3Ni} are the intrinsic hardness contributions of the α-matrix, $Al_{11}Ce_3$, and Al_3Ni phases, respectively. Only the fraction of secondary phases is used in this hardness model as a first approximation of the mechanical strength contributions, but we acknowledge that the size and distribution of secondary phases may also contribute to the strength. The intrinsic hardness of the α-matrix is composed of the contributions of Al and Mg as follows in Equation 2:

$$VHN_{matrix} = VHN_{Al} + hC_{Mg}^{n} \tag{2}$$

where VHN_{Al} is the intrinsic Vickers hardness of Al taken to be 147.1 MPa[32] while h, C, and n are constants related to solid solution strengthening of Mg with C being the concentration of Mg in wt%. Values for each parameter were found using linear regression of the predicted vs. expected values using a dataset comprising both the as-cast and homogenized button alloy data.

The final fit for the dataset showed excellent correlation as shown in Figure 10, where the final parameters were optimized by minimizing the sum of the squared errors of the data leading to a squared error for each data point below 2%. The final fit parameters for the hardness model are provided in Table 4 where the exponent n for the solid solution strengthening was derived to be 0.5759, which is close to 0.5, implying a near square root relationship for solid solution strengthening. Comparison of the relative hardness contribution of Mg and both phases as a function of their fractions is shown in Figure 11 and revealed that the greatest strengthening contribution to the total hardness was due to the solid solution strengthening contribution of Mg. The next best strengthening contribution was due to $Al_{11}Ce_3$ where the hardness contribution was about 3.86 times stronger than that of Al_3Ni. In light of the findings of hardness model combined with microstructural analysis, CNM924 was chosen for scaled-up evaluation based on having a high Mg content, possessing no primary $Al_{11}Ce_3$, and having a fine distribution of secondary phases. For this alloy, about 65% of the strength is expected to be from solid solution strengthening of Mg, while 30% of the strength contribution is from $Al_{11}Ce_3$ and 5% from Al_3Ni.

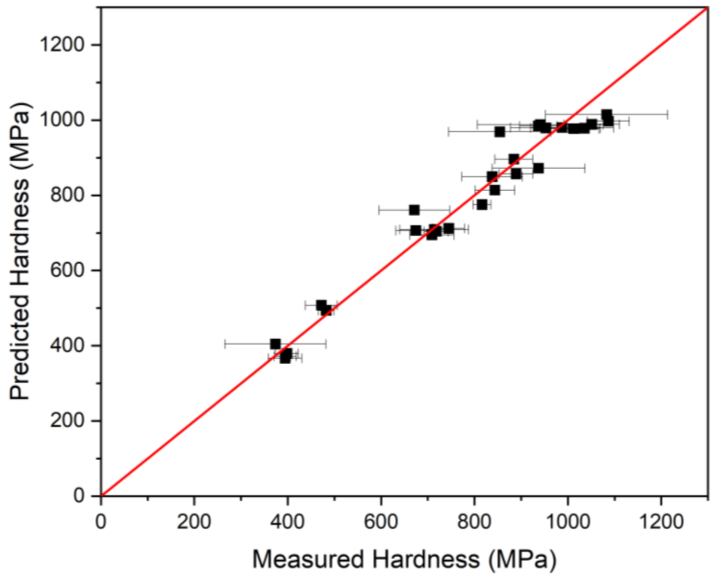

Figure 10. The predicted vs. measured hardness of constitutive hardness model for CNM alloys based on area fraction of phases.

Table 4. The derived hardness model fitting parameters.

Fit parameter	Fit value
h (MPa/wt%)	3844
n	0.5759
$VHN_{Al11Ce3}$ (MPa)	1707
VHN_{Al3Ni} (MPa)	442
VHN Al (MPa)	147.1

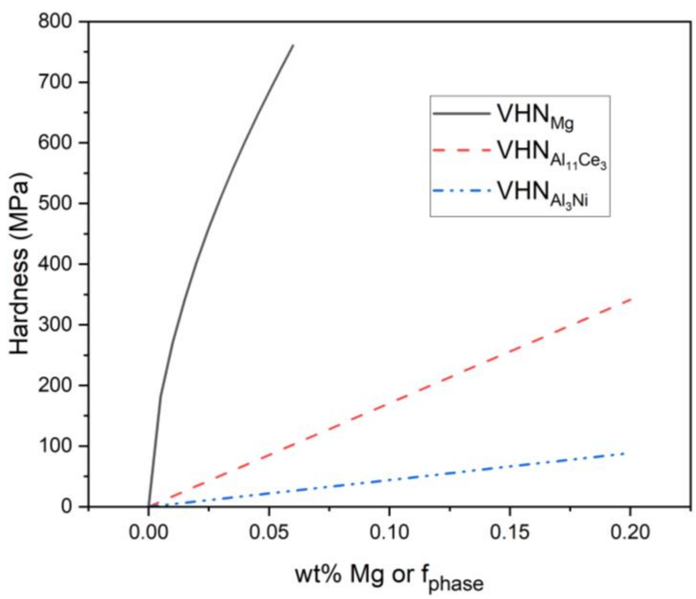

Figure 11. Individual contribution to hardness as a function of wt% Mg or phase fraction of $Al_{11}Ce_3$ and Al_3Ni.

3.3 Wedge Casting

A wedge casting of CNM924 was produced and sectioned according to the test cut plan shown in Figure 12 to provide flat dog bone tensile specimens (Figure 13) and cylinders to determine the CTE. An image sequence from the tip of the wedge to the top of the wedge is shown in Figure 14, revealing the effect of solidification rate on microstructure. A very fine distribution of lamellar eutectic phases is observed near the tip of the wedge with the image at 5 mm from the tip. This fine distribution becomes more sparse as the distance from the tip of the wedge increases, resulting in larger lamellar eutectic with greater spacing between phases.

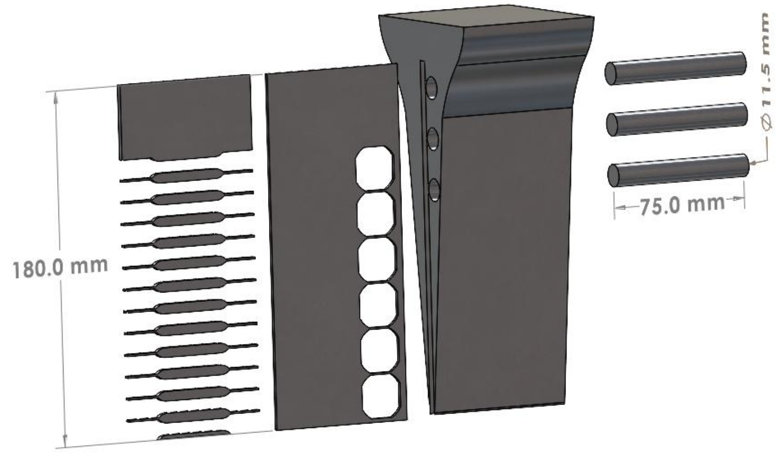

Figure 12. Test cut plan for CMN924 wedge analysis. Dog bone tensile specimens, pucks for shear punch testing (not performed), and cylinders for CTE determination are shown.

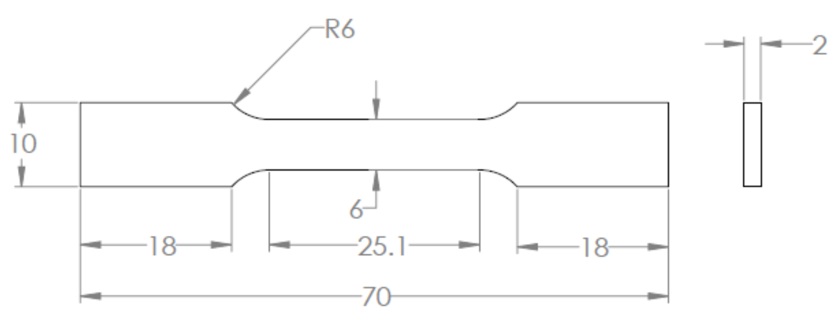

Figure 13. Schematic drawing of the modified subsize ASTM E8 flat dog bone–style tensile specimens (dimensions in millimeters).

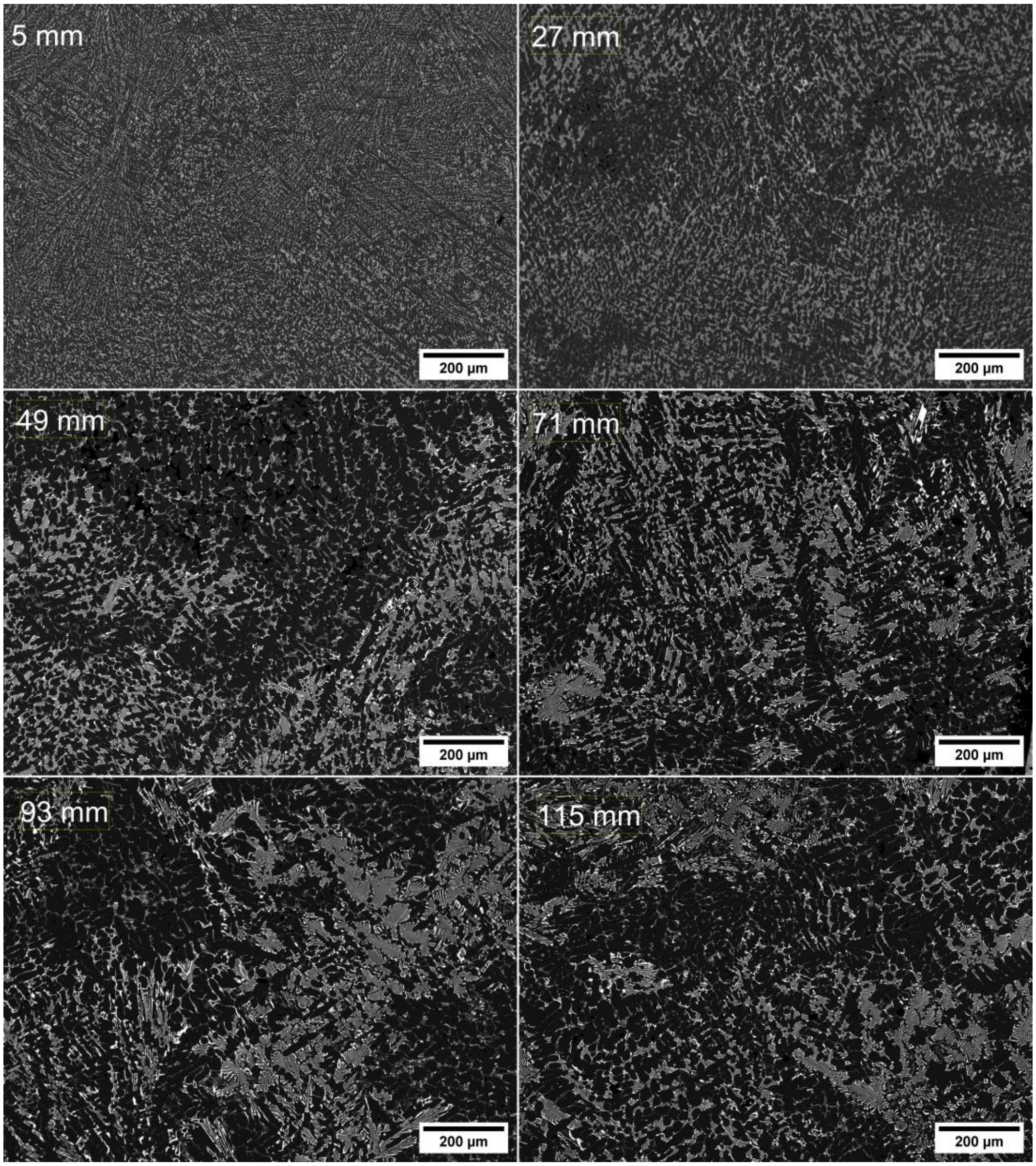

Figure 14. BSE SEM images of the CNM924 wedge casting at different distances from the tip of the wedge.

Tensile samples were tested in the as-cast condition with no homogenization heat treatment. A plot of the yield strength (YS) and ultimate tensile strength (UTS) as a function of distance from the tip of the wedge is shown in Figure 15, where a decrease in strength is observed as the solidification rate decreased. The YS measured 5 mm from the tip was 135 MPa with an UTS of 207 MPa, while the YS measured at 115 mm from the tip was 106 MPa with an UTS of 172 MPa. This is a moderate decrease in both YS and UTS compared to an Al-7Ce-6Mg-4Zn (CMZ764) alloy whose YS dropped from 294 to 135 MPa over a similar range with a decrease in UTS from 394 to 146 MPa.[33] This moderate decrease shows that CNM924 is relatively insensitive to solidification rate, making it attractive for thick section sizes in cast parts. The excellent retention of mechanical strength is likely due to the high percentage contribution of solid solution strengthening to the overall strength of the alloy as discussed in Section 3.2. Since the solid solution strength depends primarily on the fraction of matrix phase, the decrease in strength must be due to the increased size and spacing of the $Al_{11}Ce_3$ and Al_3Ni phases.

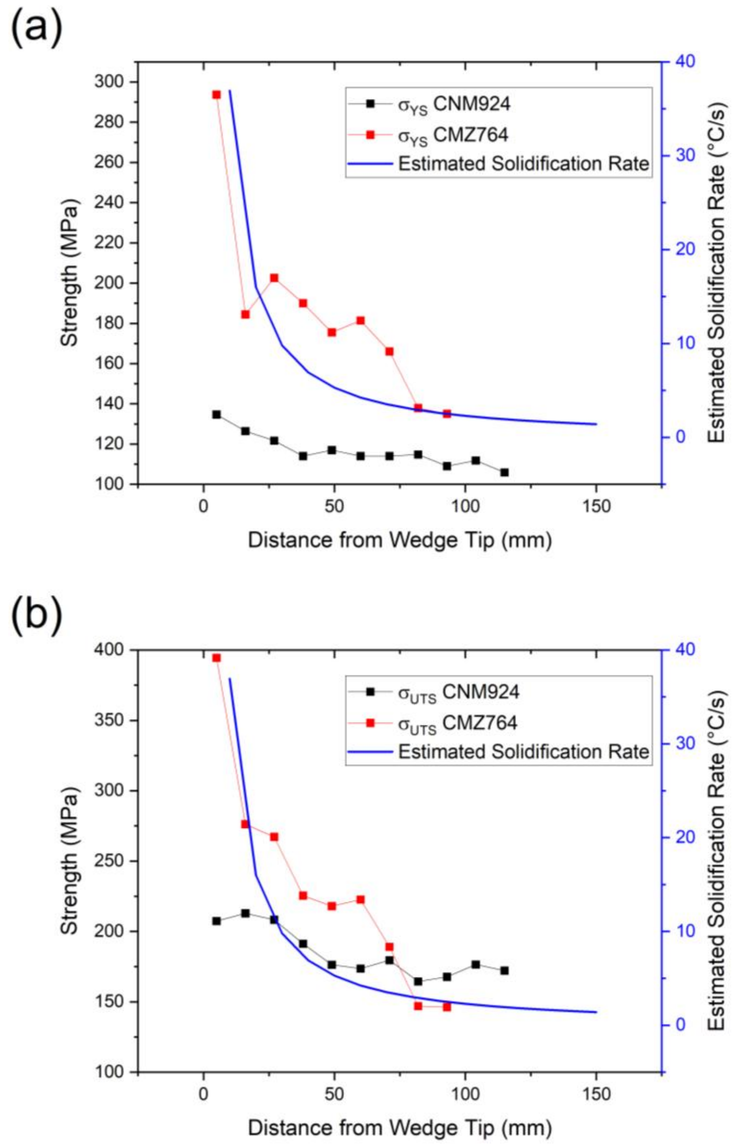

Figure 15. Plot of (a) the YS and (b) UTS of the CNM924 wedge casting as a function of distance from the tip of the wedge compared to CMZ764. Only one specimen was tested at each data point.

The results of dilatometry testing are shown in Figure 16, where the percent linear change is plotted versus temperature for CNM924 versus A356.0 and CMZ764 in the as-cast condition (F-temper). The CTE determined from linear fitting was measured to be 22.4 µm/m-°C for CNM924 for the range 20–100 °C. This value is higher than the A356.0 baseline of 21.3 µm/m-°C but less than that of CMZ764 whose CTE was measured as 22.6 µm/m-°C. At higher temperatures, the deviation between CNM924 and A356.0 increases, but the CTE remains below that of CMZ764 further demonstrating that CNM924 may be better than CMZ764 for high-temperature applications.

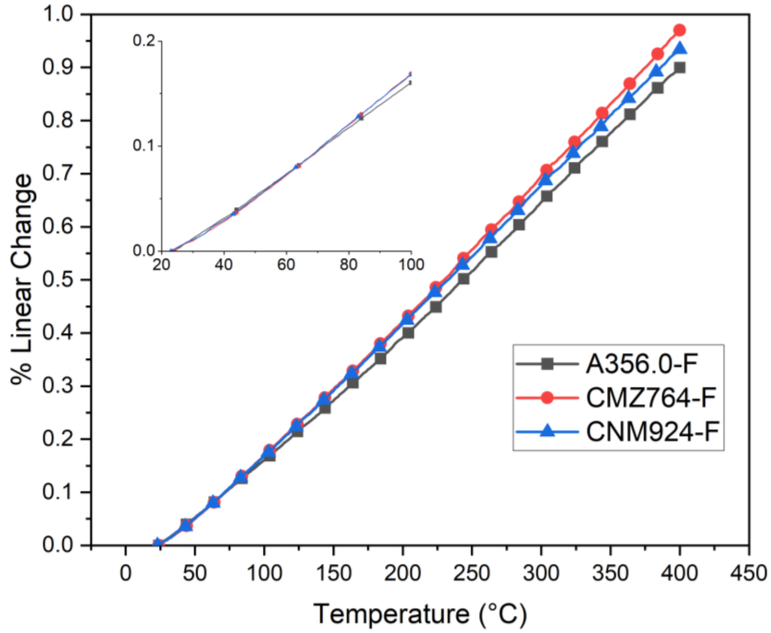

Figure 16. Percentage linear change as a function of temperature for CNM924 in the as-cast condition compared to A356.0 and CMZ764 in the as-cast state.

4. Conclusions

The Al-Ce-Ni-Mg alloy system has shown promise as a novel engineering alloy for cast applications. The following can be concluded:

- Near eutectic Al-Ce-Ni-Mg alloys are primarily strengthened by the strong solid solution strengthening effect of Mg while $Al_{11}Ce_3$ displayed a mild strengthening effect with Al_3Ni contributing a weak strengthening effect as a function of their phase fraction.
- The solidification pathway of $Al_{11}Ce_3$ phase was found to be more sensitive to the addition of Mg than Al_3Ni due to the formation of large, blocky primary $Al_{11}Ce_3$.
- A wedge casting of near eutectic alloy CNM924 showed good strength retention as a function of solidification rate due to the large contribution of Mg solid solution strengthening to the total mechanical strength.

5. References

1. Sims ZC et al. Cerium-based, intermetallic-strengthened aluminum casting alloy: high-volume co-product development. Jom. 2016;68:1940–1947.
2. Stromme ET et al. Ageless aluminum-cerium-based alloys in high-volume die casting for improved energy efficiency. Jom. 2018;70:866–871.
3. Weiss D. Improved high-temperature aluminum alloys containing cerium. J Mater Eng Perform. 2019;28:1903–1908.
4. Ng DS, Dunand DC. Aging- and creep-resistance of a cast hypoeutectic Al-6.9Ce-9.3Mg (wt.%) alloy. Mater Sci Eng A. 2020;786:139386.
5. Lv HY et al. High-performance co-continuous Al-Ce-Mg alloy with in-situ nano-network structure fabricated by laser powder bed fusion. Addit Manuf. 2022;60:103233.
6. Rakhmonov JU, Weiss D, Dunand DC. Solidification microstructure, aging evolution, and creep resistance of laser powder-bed fused Al-7Ce-8Mg (wt.%). Addit Manuf. 2022;59:103134.
7. Belov NA, Naumova EA, Eskin DG. Casting alloys of the Al-Ce-Ni system: microstructural approach to alloy design. Mat Sci Eng A-Struct. 1999;271:134–142.
8. Raghavan V. Al-Ce-Ni (aluminum-cerium-nickel). J Phase Equilib Diffus. 2009;30:265–267.
9. Wu T, Plotkowski A, Shyam A, Dunand DC. Microstructure and creep properties of cast near-eutectic Al-Ce-Ni alloys. Mat Sci Eng A-Struct. 2022;833:142551.
10. Mondolfo LF. Al–Ce–Mn aluminum–cerium–manganese system. In: Mondolfo LF, editor. Aluminum Alloys. Butterworth-Heinemann; 1976. p. 470–471.
11. Coury FG, Kiminami CS, Botta WJ, Bolfarini C, Kaufman MJ. Design and production of Al-Mn-Ce alloys with tailored properties. Mater Des. 2016;110:436–448.
12. Yang Y et al. Primary solidification of ternary compounds in Al-rich Al-Ce-Mn alloys. J Alloys Compd. 2020;844:156107.
13. Farkoosh AR, Dunand DC, Seidman DN. Solute-induced strengthening during creep of an aged-hardened Al-Mn-Zr alloy. Acta Mater. 2021;219:117255.

14. Ekaputra CN et al. Combining solution-, precipitation-, and load-transfer strengthening in a cast Al-Ce-Mn-Sc-Zr alloy. Acta Mater. 2024;266:119683. https://doi.org/10.1016/j.actamat.2024.119683

15. Sisco KD et al. Heterogeneous phase transformation pathways in additively manufactured Al-Ce-Mn alloys. J Alloys Compd. 2023;938:168541.

16. Ajantiwalay T et al. Influence of microstructural heterogeneities on small-scale mechanical properties of an additively manufactured Al-Ce-Ni-Mn alloy. Addit Manuf Lett. 2022;3:100078.

17. Kozakevich J, Stroh J, Mallouhi V, Sediako D, Weiss D. Interplay between cooling rate, microstructure, and mechanical properties of an Al–Ce–Ni–Mn alloy. In: Light Metals 2022. Springer; 2022. p. 83–91.

18. Michi RA et al. A creep-resistant additively manufactured Al-Ce-Ni-Mn alloy. Acta Mater. 2022;227:117688.

19. Emery R et al. Identification of low coefficient of thermal expansion in Al23Ce4Ni6 via combinatorial sputtering of Al-Ce-Ni-Mn thin films and upscaling to bulk materials. J Alloys Compd. 2023;968:171887.

20. Kozakevich JR, Stroh J, Sediako D, Weiss D. Solidification kinetics of an Al-Ce alloy with additions of Ni and Mn. Metals. 2023;13(3):569.

21. Michi RA et al. Additively manufactured Al-Ce-Ni-Mn alloy with improved elevated-temperature fatigue resistance. Addit Manuf. 2023;66:103442.

22. Perrin AE et al. Effect of Mn on eutectic phase equilibria in Al-rich Al-Ce-Ni alloys. J Alloys Compd. 2023;965:171350.

23. Wang W et al. Microstructure and properties of novel Al-Ce-Sc, Al-Ce-Y, Al-Ce-Zr and Al-Ce-Sc-Y alloy conductors processed by die casting, hot extrusion and cold drawing. J Mater Sci Technol. 2020;58:155–170.

24. Ekaputra CN, Rakhmonov JU, Weiss D, Mogonye JE, Dunand DC. Microstructure and mechanical properties of cast Al-Ce-Sc-Zr-(Er) alloys strengthened by Al11Ce3 micro-platelets and L12 Al3(Sc,Zr,Er) nano-precipitates. Acta Mater. 2022;240:118328.

25. Ekaputra CN et al. Combining solution-, precipitation- and load-transfer strengthening in a cast Al-Ce-Mn-Sc-Zr alloy. Acta Mater. 2024;266:119683.

26. Ekaputra CN, Mogonye JE, Dunand DC. Microstructure and mechanical properties of cast, eutectic Al-Ce-Ni-Mn-Sc-Zr alloys with multiple strengthening mechanisms. Acta Mater. 2024;274:120006.

27. Shen S et al. Architecture of bimodal interconnected structure in Al-Ce-Ni ternary alloy by super-gravity solidification and Mg doping. Mater Sci Eng A. 2025;930:148182.

28. Park H, Ekaputra CN, Dunand DC. Microstructure and creep properties of Al-7Ce-3Ni-8Mg alloys fabricated by laser powder bed fusion of powder blends. Mater Sci Eng A. 2025;926:147968.

29. Cain T, Mogonye JE. Method for rapid small-scale simulated aluminum alloy castings. DEVCOM Army Research Laboratory (US); 2021. Report No.: ARL-TN-1091.

30. Schindelin J et al. Fiji: an open-source platform for biological-image analysis. Nat Methods. 2012;9:676–682.

31. SRM 736. Copper – thermal expansion. National Institute of Standards and Technology (US); 1990 Oct 7.

32. Shercliff HR, Ashby MF. A process model for age hardening of aluminum alloys—I. The model. Acta Metall Mater. 1990;38:1789–1802.

33. Cain TW, Mogonye JE. Development of Al–Ce–Mg–Zn-based alloys. DEVCOM Army Research Laboratory (US); 2024. Report No.: ARL-TR-9980.

List of Symbols, Abbreviations, and Acronyms

Al	Aluminum
Ar	Argon
ARL	Army Research Laboratory
BN	Boron Nitride
BSE	Backscattered Electron
CAMI	Coated Abrasive Manufacturers Institute
Ce	Cerium
Co	Cobalt
CTE	Coefficient of Thermal Expansion
Cu	Copper
DEVCOM	U.S. Army Combat Capabilities Development Command
EDS	Energy-Dispersive Spectroscopy
FCC	Face-Centered Cubic
He	Helium
Mg	Magnesium
Mn	Manganese
Ni	Nickel
Sc	Scandium
SEM	Scanning Electron Microscope
SiC	Silicon Carbide
SRM	Standard Reference Material
UTS	Ultimate Tensile Strength
VIM	Vacuum Induction Melting
wt%	Weight Percent
XRD	X-ray Diffraction
YS	Yield Strength

Zn	Zinc
Zr	Zirconium

1 (PDF)	DEFENSE TECHNICAL INFORMATION CTR DTIC OCA
1 (PDF)	DEVCOM ARL FCDD RLB CB TECH LIB